Available online at www.sciencedirect.com
ScienceDirect
Microporous and Mesoporous Materials 100 (2007) 154–159
MICROPOROUS AND MESOPOROUS MATERIALS
www.elsevier.com/locate/micromeso

Anion impurities in porous alumina membranes: Existence and functionality

D.H. Fan, G.Q. Ding, W.Z. Shen *, M.J. Zheng

Laboratory of Condensed Matter Spectroscopy and Opto-Electronic Physics, Department of Physics, Shanghai Jiao Tong University, 1954 Hua Shan Road, Shanghai 200030, PR China

Received 7 September 2006; received in revised form 14 October 2006; accepted 16 October 2006
Available online 29 November 2006

Abstract

We have carried out a detailed investigation on $C_2O_4^{2-}$ anion impurities in self-organized porous alumina membranes (PAMs) prepared by a two-step electrochemical anodization process in oxalic acid solutions. The employment of the energy dispersive spectroscopy, high resolution transmission electron microscope and infrared absorption spectra has demonstrated the existence and nonuniform distribution of the $C_2O_4^{2-}$ anions in the PAM sidewalls. The variation of the COO^- stretching vibration and CO_2 absorption bands indicates that annealing can lead to the decrease of the $C_2O_4^{2-}$ concentration in the PAMs due to the decomposition of impurity groups related to $C_2O_4^{2-}$. We have further presented clear functionality that the $C_2O_4^{2-}$ anions have played key roles in the refractive index and absorption coefficient of the PAMs, and the surface morphology and crystallization of the deposited ZnO nanopore arrays.

PACS: 81.16.Rf; 82.45.Yz; 61.72.Ww; 81.07.−b

Keywords: Anion impurities; Porous alumina membranes; Nanostructure materials

1. Introduction

Self-organized porous alumina membranes (PAMs) prepared by a two-step electrochemical anodization process have received increasing attention due to their potential application in the fields of magnetic storages [1], functional electrodes [2], solar cells [3], carbon nanotubes [4], catalysts [5], photonic crystals [6], and electroluminescence display devices [7], as well as their unique structure properties and relatively easy and low-cost processing [8]. So far, highly-ordered PAMs with the pore diameters of 25–300 nm and thickness of 50–200 nm have been successfully prepared. In particular, ultrathin free-standing PAMs [9] have been fabricated and can be transformed onto different substrates as templates to synthesize the nanomaterials, such as nanodot arrays and nanopore arrays [8,10].

It should be noted that during the preparation of PAMs, there are oxalic impurities in PAMs due to the competition between the water-splitting reaction ($3/2H_2O \rightarrow 3H^+ + 3/2O^{2-}$) and dissociation of acids ($HC_2O_4^- \rightarrow C_2O_4^{2-} + H^+$) to form conjugate base anions, which can replace O^{2-} in the oxide as substitution or contamination impurities [11–13]. Mardilovich et al. [14] have confirmed that oxalic impurities of PAMs during the calcinations could decompose and form other impurities. A limited investigation has demonstrated that the anion impurities play an important role not only in the optoelectronic properties of the PAM itself, but also in the deposition of nanomaterials. Yamamoto et al. [15] have proposed, as early as in 1981, that the oxalic impurities incorporated in PAMs can be transformed into luminescent centers, showing a blue photoluminescence (PL) band around 470 nm. We have identified that the blue PL band originates from the coactions of the singly ionized oxygen vacancies and the luminescent centers transformed from oxalic impurities

* Corresponding author. Fax: +86 21 54743242.
E-mail address: wzshen@sjtu.edu.cn (W.Z. Shen).

1387-1811/$ - see front matter © 2006 Elsevier Inc. All rights reserved.
doi:10.1016/j.micromeso.2006.10.025

[16]. Choi et al. [17] have observed the relationship between the anion content and the dielectric constant of PAMs: the more anions are incorporated in the alumina, the lower the dielectric constant. Very recently, we have reported that, during the sputtering of ZnO, these localized negative charges will attract Zn^{2+} ions, resulting in the formation of well-ordered semiconducting ZnO nanopore arrays on top of the PAMs [10].

In this paper, we have employed the structural and optical measurements to reveal the existence of the $C_2O_4^{2-}$ anions and testify the functionality of the anion impurity concentration on the refractive index and absorption coefficient of the PAM itself, and the surface morphology and crystallization of the synthesized ZnO nanopore arrays. The present work establishes an experimental base for the overall understanding the role of the $C_2O_4^{2-}$ anions.

2. Experimental details

PAMs were fabricated through a typical two-step anodizing electrochemical procedure with high-purity (99.999%) aluminum foil degreased in acetone as the anode in 0.3 M oxalic acid ($H_2C_2O_4$) electrolyte. The first anodization lasted for 2 h under the constant anodizing voltage of 40 V and electrolyte temperature of 10 °C. The specimens were then immersed in a mixture of 6.0 wt% H_3PO_4 and 1.8 wt% H_2CrO_4 at 60 °C for 4 h to remove the alumina layers. After the second 5 min anodization under the same conditions as the first one, highly-ordered PAMs were formed. The unoxided aluminum was removed in a saturated $CuSO_4$ solution at ambient temperature. The specimens were immersed into the 6% H_3PO_4 at 30 °C to remove the barrier layer and to enlarge the nanopore size. After several times washing in deionized water, PAMs with a thickness of ~500 nm and porosity of ~0.16 were transferred onto fine-polished *n*-type Si (0 0 1) substrates. The post-annealing of PAMs was carried out in vacuum atmosphere for 3 h using vacuum annealing furnace. The annealing temperature varied from 400 to 900 °C. The ramp-up rate was fixed at 15 °C/min and the samples were naturally cooled down after heating. We found that during the annealing process, the PAMs would not get away from the substrates because of the van der Waals bonding between the Si substrates and PAMs.

3. Results and discussion

Fig. 1a shows the energy dispersive spectroscopy (EDS) (JEOL JEM-2100F) of the as-deposited PAMs. The PAMs mainly consist of two elements of aluminum and oxygen with little carbon due to strong Kα peaks of Al at 1.5 keV and O at 0.5 keV, together with weak Kα one of C at 0.26 keV. It is proposed that the oxalic impurities moving towards the anode during anodization can partly replace O^{2-} and OH^-, which leads to the formation of $C_2O_4^{2-}$ anions in PAMs [11–13]. The observation of C in the EDS spectrum indicates the presence of the $C_2O_4^{2-}$ anions in the PAMs. The distribution of the above-mentioned elements in the PAM sidewalls can be further experimentally examined by the EDS line scan with a spatial resolution approaching 1.5 nm. The inset of Fig. 1a displays the normalized intensity of these three elements along the longest arrow in Fig. 1b.

During the anodization, part of Al^{3+} ions formed at metal/oxide interface ($Al \rightarrow Al^{3+} + 3e^-$) drift through the oxide layer, and eject into the solution at the oxide/electrolyte interface [12]. The closer to electrolyte, the more Al^{3+} ions in PAMs migrate into the electrolyte due to lower resistance, which is responsible for the higher aluminum content in the inner layer. Oxygen containing ions (O^{2-}/OH^-) migrates from the electrolyte through oxide layer to the metal/oxide interface [12,18], resulting in the oxidation of aluminum in the PAMs. Since the oxygen in the PAMs mainly exists as alumina, the presence of more alumina in the inner layer brings about larger oxygen content. In contrast, due to the lager size and lower mobility of oxalic anions compared with O^{2-} and OH^- [11,13], the $C_2O_4^{2-}$ anions will decrease from the sidewall outer to inner layers (Fig. 1b). This kind of distribution has been clearly demonstrated by the profile of carbon element in the inset of Fig. 1a. We therefore have presented experimental evidence of the nonuniform distribution of Al, O, and $C_2O_4^{2-}$ anions in the sidewalls, adding the knowledge of deep understanding the PAMs.

The existence of the $C_2O_4^{2-}$ anion impurities can also be confirmed by the high resolution transmission electron microscope (HRTEM) image. Fig. 1b clearly exhibits the duplex layer structures for the PAM sidewalls, with the dark inner layer and relatively bright outer layer. The different contrast is the results of more anion-contaminated outer layer and the inner layer of high alumina density. Similar porous alumina structure has also been observed by Nielsch et al. [19].

Furthermore, the infrared vibrational measurements have the ability to reveal the existence of $C_2O_4^{2-}$ impurities in the PAMs, and the variation of the absorption peak intensity can reflect the corresponding impurity concentration. During the anodization, $C_2O_4^{2-}$ ions migrating into PAMs can form impurity groups related to (_ _‖_‖_ _) [11]. In those groups, C═O and C–O bonds with the same C atom will average into two equivalent carbon–oxygen bonds ((− ⟨ −)). The strong coupling between the two equal bonds results in the COO^- asymmetrical stretching vibration asym. str. from 1558 to 1593 cm^{-1} and relatively weak COO^- symmetrical stretching vibration sym. str. from 1403 to 1455 cm^{-1} [20,21]. Fig. 2a displays the room-temperature infrared absorption spectra of the ultrathin PAMs annealed at different temperatures, which were performed on a Nicolet Nexus 870 Fourier transform infrared spectrometer. The observation of ~1565 and 1445 cm^{-1} absorption bands in the as-deposited PAMs corresponds well with these two vibration modes in the impurity groups related to $C_2O_4^{2-}$. The absorption peak of 1100 cm^{-1} is due

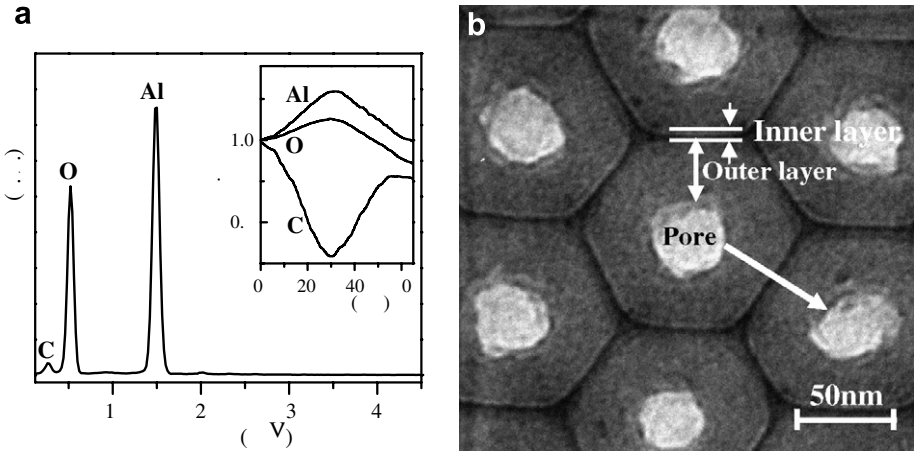

Fig. 1. (a) EDS spectrum and (b) HRTEM image of the as-deposited PAMs. The inset in (a) is the EDS line scan along the longest arrow in (b).

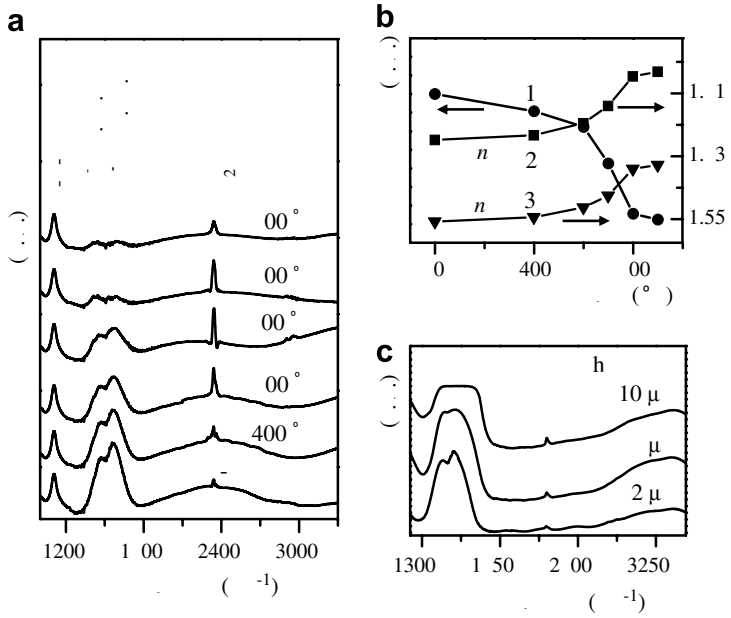

Fig. 2. (a) Room-temperature infrared absorption spectra of the as-prepared and annealed PAMs at different temperatures for 3 h. Curve 1 in (b) is the integrated intensity of the COO^- stretching modes in (a), and curves 2 and 3 in (b) are the annealing temperature-dependent refractive index n_a of the host alumina and effective refractive index n_{eff} of the PAMs at 546 nm, respectively. (c) The infrared absorption spectra of the as-deposited PAMs with different thicknesses.

to the stretching vibrations of Si–O–Si in the oxidized Si substrate [22], i.e., not related with the PAMs.

From Fig. 2a, we can also observe the variation of the COO^- absorption band intensity with the increase of annealing temperature. To clearly reveal the effect, we show in Fig. 2b (curve 1) the integrated intensity of the COO^- stretching modes from 1290 to 1760 cm^{-1}. It is found that the integrated intensity decreases with the increase of annealing temperature, which indicates that annealing can lead to the decrease of the $C_2O_4^{2-}$ content due to the decomposition of the impurity groups related to $C_2O_4^{2-}$. Especially, when the annealing temperature increases from 600 to 800 °C, the integrated intensity decreases rapidly, revealing the large decomposition of the $C_2O_4^{2-}$ impurity groups and therefore sharp decrease of the $C_2O_4^{2-}$ anion content in the PAMs. The above arguments can also be testified by the shift of the COO^- (sym. str.) absorption peak in Fig. 2a. The COO^- (sym. str.) redshifts with increasing annealing temperature below 800 °C, whereas it keeps almost unchanged under annealing at and above 800 °C, since stable impurities, such as aluminum-carboxylate complex [15], has gradually been formed in the PAMs due to the decomposition of the impurity groups related to $C_2O_4^{2-}$. For the 2342 cm^{-1} absorption peak in Fig. 2a, it had been reported that this peak is attributed to the formation of CO_2 inside the PAMs rather than the CO_2 from the air [14,23]. The increase of the CO_2 absorption peak intensity further confirms that annealing can lead

to the decrease of the $C_2O_4^{2-}$ concentration due to the decomposition of impurity groups related to the $C_2O_4^{2-}$ in PAMs [16]. However, the CO_2 gasification in PAMs at high annealing temperatures will decrease its intensity.

It is worthy to note that the lineshape of the observed COO^- stretching modes depends on the thickness of the PAMs. Fig. 2c shows the infrared absorption spectra of the as-deposited PAMs with different thicknesses. It is clear that with the increase of thickness, both the two COO^- absorption peaks broaden gradually, become undistinguishable and form a single broad absorption band in the thick PAMs. The above phenomena can be well explained by the fact that the amount of the impurity groups related to the $C_2O_4^{2-}$ in thick PAMs is more than that in the thin ones, resulting in the strong absorption in the range of 1400–1700 cm^{-1}. This also accounts for the different observation of the related absorption in Ref. [16] (with thick PAMs). The observed variation of the COO^- absorption peaks with different PAM thicknesses indicates that the infrared absorption spectra of ultrathin PAMs can precisely reflect the microstructural characteristics of the PAMs.

In addition to the vibrational bands, the different $C_2O_4^{2-}$ concentrations in the PAMs will play key roles in both the optical properties of the PAM itself and the surface morphology and crystallization of the deposited nanomaterials. By using the modified four-layer-medium transmission model (i.e., air/PAM/substrate/air here) and the fitting procedure described in Ref. [24], we have determined the wavelength-dependent refractive index and absorption coefficient of the host alumina in the PAMs below the band gap from the observed interference fringes in the optical transmission spectra. Fig. 3a shows the experimental transmission spectra (filled circles) of the PAMs annealed at different temperatures, which were performed on a Jobin Yvon 460 monochromator, together with the corresponding calculated spectra (solid curves).

To achieve the reliability of the transmission model during the fitting, we have adopted the real thickness of the PAMs measured by scanning electron microscope (SEM), and considered the PAM's porosity since PAMs are composed of alumina and air. From Fig. 3a, we can observe that the theoretical interference fringes fit well with the experimental data. Fig. 3b gives the yielded wavelength-dependent refractive index n_a of the host alumina in the PAMs annealed at different temperatures. The refractive index n_a in the as-deposited PAMs is ~1.65 at 546 nm, in good agreement with the reported value of $\sim 1.64 \pm 0.01$ obtained by the optical waveguide method [25]. We have further shown in Fig. 2b (curve 2) the annealing temperature-dependent refractive index n_a of the host alumina at 546 nm, where the refractive index n_a is found to increase with the annealing temperature. Choi et al. have reported that the anion-incorporated alumina had lower dielectric constant compared to that of the pure alumina [17]. The dielectric constant of alumina in the visible and infrared ranges is approximately equivalent to the square of the

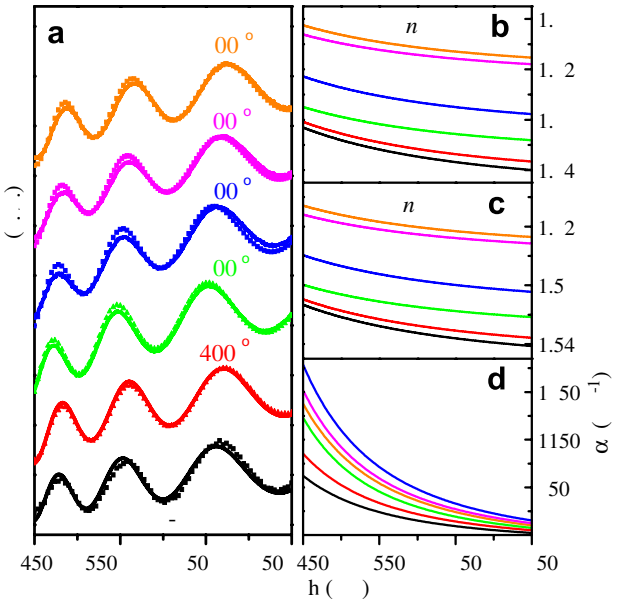

Fig. 3. (a) Experimental (filled circles) and calculated (solid curves) transmission spectra of the as-deposited and annealed PAMs in the visible wavelength range. Yielded wavelength-dependent (b) refractive index n_a of the host alumina, (c) effective refractive index n_{eff} of the PAMs, and (d) absorption coefficient α of the host alumina.

refractive index due to the low absorption coefficient. Therefore, the decrease of the $C_2O_4^{2-}$ anion concentration with the increase of annealing temperature (see curve 1 of Fig. 2b, the integrated intensity of the COO^- mode absorption) results in the increase of the refractive index of the host alumina.

There is another refractive index characterizing the PAMs: the effective refractive index n_{eff}, which differs from the refractive index n_a of the host alumina and varies with the porosity. Fig. 3c displays the wavelength-dependent effective refractive index n_{eff} of the annealed PAMs, calculated by Bruggeman's effective medium approximation [26]. The effective refractive index n_{eff} of the as-prepared PAMs is found to be 1.54 at 750 nm, which is also consistent with the reported result of 1.53 in Ref. [27]. With the increase of annealing temperature, n_{eff} has the same variation trend as n_a (curve 3 in Fig. 2b), further demonstrating the role of the anion impurities in the optical properties of the PAMs.

The yielded wavelength-dependent absorption coefficient α below the band gap of the PAMs in Fig. 3d also reflects the variation of the anion impurities in the PAMs. In the PAMs annealed below 700 °C, with the increase of the annealing temperature, more new defects will be introduced due to the increased decomposition of the anion impurities, leading to the formation of more defect states located in the band gap. As a result, the absorption coefficient will increase with the annealing temperature. However, high temperature (above 700 °C) annealing will cause the crystallization of the amorphous PAMs [16], and therefore decrease the absorption coefficient below the band gap. Although the decomposition of the anion

impurities enhances with the annealing temperature, it is clear that the crystallization effect dominates the variation of the absorption coefficient, since the absorption coefficient is found to decrease with the increase of the annealing temperature above 700 °C.

The $C_2O_4^{2-}$ anion impurities affect not only the optical properties of the PAM itself but also the deposition of nanomaterials. Here we systematically investigate the dependence of the synthesized ZnO nanopore arrays on the $C_2O_4^{2-}$ anion concentration in the PAMs. The process is deposition of ZnO particles onto the PAMs via a radio-frequency (13.56 MHz) magnetron sputtering system with a sintered ceramic ZnO target (99.99%, purity) as source material. The PAM serves as a template for the fabrication of ZnO nanopore arrays [10]. After being annealed at different temperatures, the annealed PAMs were carried into the sputtering chamber, so that the deposition was done under the same conditions for the ZnO nanopore arrays. The deposition pressure, substrate–target distance, sputtering time and sputtering power were 2 Pa, 4 cm, 30 min and 100 W, respectively. Fig. 4 displays the field-emission SEM (Philips XL30FEG) images of the fabricated ZnO nanopore arrays on the as-deposited and annealed PAMs. It is clear that ordered ZnO nanopore arrays have been formed on the top surface of the as-deposited PAMs (Fig. 4a) with the pattern identical to that of PAMs, and every hexagonal ZnO nanopore is composed of six ZnO grains. Ding et al. [10] have attributed the formation of highly-ordered ZnO nanopore arrays to the attraction between the localized negative charges in PAMs and Zn^{2+} ions.

When the PAMs were annealed below 400 °C, the morphology of the sputtered ZnO nanopores was basically unchanged. With the annealing temperature increased to 600–700 °C, the yielded ZnO nanopores were no more circular and the cells of ZnO nanopores were not hexagonal any more, as shown in Fig. 4b and c. Many ZnO grains (much more than six) were irregularly deposited on the surface of a single PAM cell, and the regularity of the ZnO nanopore arrays decreases obviously. Especially, under the PAMs annealed at 900 °C, the regularity of ZnO nanopores becomes very poor and even parts of nanopores are jammed by ZnO particles (Fig. 4d).

Apart from the $C_2O_4^{2-}$ anion concentration, the as-deposited and annealed PAMs do not have obvious difference in the surface morphology and thickness. So it is reasonable to believe that the anion impurities in the PAMs have the ability to affect the deposition of nanomaterials. Compared with the as-prepared PAMs, the annealed PAMs were with less anion impurity content due to the pyrolysis, leading to the weaker attraction of Zn^{2+} ions during the sputtering. This is the main reason why the morphology of the ZnO nanopore arrays gets worse as the annealing temperature increases.

X-ray diffraction (XRD) measurements can further testify the effect of the anion impurities in PAMs on the crystallization of these ZnO nanopore arrays. Fig. 5 shows the XRD spectra (under a Bruker D8 ADVANCE system with

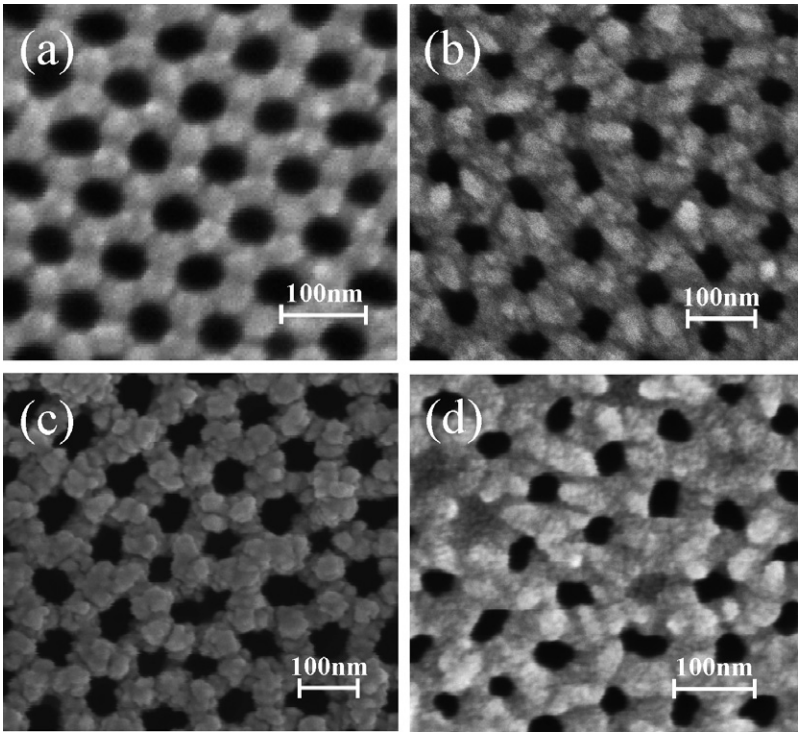

Fig. 4. Field-emission SEM images of the ZnO nanopore arrays on top of the (a) as-deposited PAMs, and annealed PAMs at (b) 600 °C, (c) 700 °C, and (d) 900 °C.

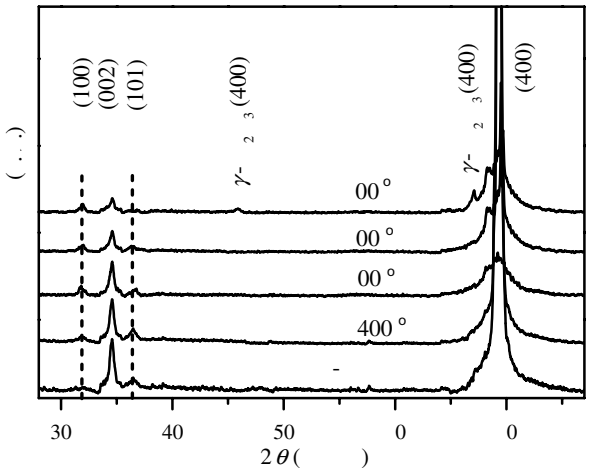

Fig. 5. XRD spectra of the ZnO nanopore arrays on top of as-deposited and annealed PAMs at different temperatures.

a Cu Kα of 1.5406 Å, step size of 0.02°/s) of the ZnO nanopore arrays on top of the PAMs annealed at different temperatures. The XRD spectrum of the ZnO nanopore arrays on the as-prepared PAM exhibits a strong (002) orientation peak and two weak (100) and (101) peaks [28] without any other diffraction peaks. As we know, the higher the relative intensity of the strongest (002) diffraction peak is, the better the ZnO crystal quality is. It is found that the ZnO (002) peak intensity gradually decreases with the increase of the annealing temperature, which clearly indicates that lower anion impurity concentration leads to the worse crystal quality. In the PAMs annealed at 900 °C, besides the weak ZnO diffraction peaks, two γ-Al_2O_3 diffraction peaks appear at $2\theta = 45.92°$ and 67.06° [29], confirming that the high temperature annealing can lead to the crystallization of the PAMs [16].

4. Conclusions

In summary, we have demonstrated the existence and nonuniform distribution of the $C_2O_4^{2-}$ anion impurities in the PAM sidewalls by the aid of EDS, HRTEM, and infrared absorption measurements. The $C_2O_4^{2-}$ anion impurity concentration in the PAMs is found to be controllable by the post-annealing at different temperatures due to the decomposition of impurity groups related to $C_2O_4^{2-}$. With the increase of annealing temperature for the PAMs, more impurity groups related to $C_2O_4^{2-}$ are decomposed and $C_2O_4^{2-}$ impurity concentration in PAMs decreases. We have further investigated in detail the functionality of the anion impurities in both the optical properties of the PAM itself and the surface morphology and crystallization of the deposited nanostructured materials. It is found that the decrease of the $C_2O_4^{2-}$ impurity concentration results in the increase of the refractive index and absorption coefficient of the PAMs, and worse regularity and crystal quality of the synthesized ZnO nanopore arrays. The deep understanding the role of the $C_2O_4^{2-}$ anion impurities paves the way for the better employment of the PAMs in the fabrication of novel nanomaterials.

Acknowledgments

This work was supported by the National Natural Science Foundation of China (Grant Nos. 10674094, 50572064 and 60576067), Shanghai Municipal Commission of Science and Technology Major Projects of 05DJ14003, 05QMH1411 and 06JC14039, and the National Minister of Education Program for Changjiang Scholars and Innovative Research Team in University (PCSIRT).

References

[1] K. Nielsch, R.B. Wehrspohn, J. Barthel, J. Kirschner, U. Gösele, S.F. Fischer, H. Kronmüller, Appl. Phys. Lett. 79 (2001) 1360.
[2] M.J. Tiemey, C.R. Martin, J. Electrochem. Soc. 137 (1990) 3789.
[3] R. Karmhag, T. Tesfamichael, E. Wäckelgård, G.A. Niklasson, M. Nygren, Sol. Energy 68 (2000) 329.
[4] G. Che, B.B. Lakshmi, E.R. Fisher, C.R. Martin, Nature 393 (1998) 346.
[5] G. Che, B.B. Lakshmi, C.R. Martin, E.R. Fisher, R.S. Ruoff, Chem. Mater. 10 (1998) 260.
[6] H. Masuda, M. Ohya, H. Asoh, M. Nakao, M. Nohtomi, T. Tamamura, Jpn. J. Appl. Phys. 38 (1999) L1403.
[7] L. Mizuki, Y. Yamamoto, T. Yoshino, N. Baba, J. Metal. Surf. Finish. Soc. Jpn. 38 (1987) 561.
[8] H. Chik, J.M. Xu, Mater. Sci. Eng. R 43 (2004) 103.
[9] G.Q. Ding, M.J. Zheng, W.L. Xu, W.Z. Shen, Nanotechnology 16 (2005) 1285.
[10] G.Q. Ding, W.Z. Shen, M.J. Zheng, D.H. Fan, Appl. Phys. Lett. 88 (2006) 103106.
[11] F.Y. Li, L. Zhang, R.M. Metzger, Chem. Mater. 10 (1998) 2470.
[12] O. Jessensky, F. Müller, U. Gösele, Appl. Phys. Lett. 72 (1998) 1173.
[13] Y. Xu, G.E. Thompson, G.C. Wood, B. Bethune, Corros. Sci. 27 (1987) 83.
[14] P.P. Mardilovich, A.N. Govyadinov, N.I. Mukhurov, J. Membrane Sci. 98 (1995) 131.
[15] Y. Yamamoto, N. Baba, S. Tajima, Nature 289 (1981) 572.
[16] W.L. Xu, M.J. Zheng, S. Wu, W.Z. Shen, Appl. Phys. Lett. 85 (2004) 4364.
[17] J. Choi, Y. Luo, R.B. Wehrspohn, R. Hillebrand, J. Schilling, U. Gösele, J. Appl. Phys. 97 (2003) 4757.
[18] V.P. Parkhutik, V.I. Shershulsky, J. Phys. D: Appl. Phys. 25 (1992) 1258.
[19] K. Nielsch, J. Choi, K. Schwirn, R.B. Wehrspohn, U. Gösele, Nano Lett. 2 (2002) 278.
[20] Y. Omura, Spectroc. Acta Pt. A 54 (1998) 507.
[21] M. Mizuguchi, M. Nara, K. Kawano, K. Nitta, FEBS Lett. 417 (1997) 153.
[22] X.Y. Chen, W.Z. Shen, H. Chen, R. Zhang, Y.L. He, Nanotechnology 17 (2006) 595.
[23] T. Gao, G.W. Meng, L. Zhang, J. Phys.: Condens. Matter 15 (2003) 2071.
[24] H. Chen, M.H. Gullanar, W.Z. Shen, J. Cryst. Growth 260 (2004) 91.
[25] S. Nakamura, M. Saito, L.F. Huang, M. Miyagi, K. Wada, Jpn. J. Appl. Phys. 31 (1992) 3589.
[26] T.D. Kang, H. Lee, S.J. Park, J. Jang, S. Lee, J. Appl. Phys. 92 (2002) 2467.
[27] M. Saito, M. Shibasaki, S. Nakamura, M. Miyagi, Opt. Lett. 19 (1994) 710.
[28] D.H. Fan, Z.Y. Ning, M.F. Jiang, Appl. Surf. Sci. 245 (2005) 414.
[29] R. Krishnan, S. Dash, C.B. Rao, R.V.S. Rao, A.K. Tyagi, B. Raj, Scr. Mater. 45 (2001) 693.